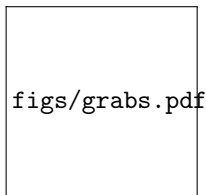


Graphical Abstract

Surface-resolved dynamic simulation of charged non-spherical particles

CV Radhakrishnan, Han Theh Thanh, CV Rajagopal, Rishi T.



Highlights

Surface-resolved dynamic simulation of charged non-spherical particles

CV Radhakrishnan,Han Theh Thanh,CV Rajagopal,Rishi T.

- Research highlights item 1
- Research highlights item 2
- Research highlights item 3

Surface-resolved dynamic simulation of charged non-spherical particles^{★,★★}

Sir CV Radhakrishnan^{a,c,*1} (Researcher), Han Theh Thanh^{b,d}, CV Rajagopal Jr^{b,c,2} (Co-ordinator) and Rishi T^{a,c,*,1,3}

^aElsevier B.V., Radarweg 29, 1043 NX Amsterdam, The Netherlands

^bSayahna Foundation, Jagathy, Trivandrum 695014, India

^cSTM Document Engineering Pvt Ltd., Mepukada, Malayinkil, Trivandrum 695571, India

ARTICLE INFO

Keywords:

Electrostatic interaction
Non-spherical particles
Boundary element method
Discrete element method
Reduced stiffness

ABSTRACT

We present a numerical method for dynamic simulations of dielectric non-spherical particles carrying electrical charges. The boundary element method (BEM) is employed to calculate the surface charge distribution, based on which the electrostatic interactions among particles are computed. The method of generalized minimum residual (GMRES) incorporated with the fast multipole method (FMM) is adopted to perform efficient electrostatic calculation. When particles collide with each other, the contact forces and torques are included using the Hertzian contact model, which provides detailed information of each collision process. Besides, the reduced stiffness is applied to increase the collision time step, which significantly accelerates the simulation. The electrostatic forces between two dielectric spheres obtained from different models are compared to show the relative importance of the induced higher-order multipoles. The electrostatic force between a pair of ellipsoids are also given to discuss the effect of the non-spherical shape. Then the dynamic simulations of the collision between a particle and an aggregate are performed with the evolution of the electrostatic interaction and the interparticle collision well captured. This comprehensive model shows good applicability in reproducing typical collision outcomes, e.g., sticking, fragmentation and rearrangement, which could reveal the fundamentals of charged particle dynamics.

1. Introduction

The electrostatic interactions widely exist in particulate systems. Under certain conditions, the electrostatic interactions become comparable to or even stronger than other interactions, which leads to significant changes in particle behavior. As a result, the electrostatic interactions play a key role in natural processes such as the formation of planet (Lee, Waitukaitis, Miskin and Jaeger, 2015; Steinpilz, Joeris, Jungmann, Wolf, Brendel, Teiser, Shinbrot and Wurm, 2020), sediment transport (Harper, McDonald, Dufek, Malaska, Burr, Hayes, McAdams and Wray, 2017) and ash aggregation in volcanic plumes (Telling, Dufek and Shaikh, 2013), as well as industrial applications like suspensions of charged colloidal particles (Allahyarov, Zaccarelli, Sciortino, Tartaglia and Löwen, 2007), particulate matters control (Jaworek, Marchewicz, Sobczyk, Krupa and Czech, 2018) and powder build-up in conveying tubes (Song and Mehrani, 2017).

In systems containing a large number of particles, dielectric particles are often treated as point charges for simplicity, which leads to the pairwise Coulomb interaction (Lu and Shaw, 2015; Di Renzo and Urzay, 2018; Steinpilz et al.,

* This document is the results of the research project funded by the National Science Foundation.

** The second title footnote which is a longer text matter to fill through the whole text width and overflow into another line in the footnotes area of the first page.

This note has no numbers. In this work we demonstrate a_b the formation Y_1 of a new type of polariton on the interface between a cuprous oxide slab and a polystyrene micro-sphere placed on the slab.

* Corresponding author

** Principal corresponding author

 cvr_1@tug.org.in (C. Radhakrishnan); cvr3@sayahna.org (C. Rajagopal); rishi@stmdocs.in (R. T.)

 www.cvr.cc, cvr@sayahna.org (C. Radhakrishnan); www.sayahna.org (C. Rajagopal); www.stmdocs.in (R. T.)

ORCID(s): 0000-0001-7511-2910 (C. Radhakrishnan)

¹This is the first author footnote. but is common to third author as well.

²Another author footnote, this is a very long footnote and it should be a really long footnote. But this footnote is not yet sufficiently long enough to make two lines of footnote text.

2020; Ruan, Chen and Li, 2021). When particles are close to each other, however, the influence of the induced charge becomes important, so a more accurate model is in need. In various simulations, the induced dipole model has been included, which characterizes the slight relative shift of the positive and negative charge induced by the external field. By using the induced dipole model, abundant phenomena have been reported in both granular flows (Kolehmainen, Ozel, Gu, Shinbrot and Sundaresan, 2018) and particle-laden flows (Liu, Marshall, Li and Yao, 2010) revealing the essential influence of particle polarization.

Nevertheless, the dipole moment is only the first-order approximation of the charge non-uniformity on the particle surface, which limits its accuracy when the induced higher-order multipoles are important (Barros and Luijten, 2014; Lee et al., 2015). Hence, for decades researchers have been devoted to finding more precise descriptions of the electrostatic interactions. For simple geometries such as a pair of spheres or a sphere and a wall, analytic solutions have been proposed to calculate the electrostatic interactions. Typical examples include the image charge method (Lindell, Sten and Nikoskinen, 1993; Ohshima, 1995; Ohshima, Mishonova and Alexov, 1996) and the re-expansion method (Washizu, 1993; Nakajima and Sato, 1999; Bichoutskaia, Boatwright, Khachatourian and Stace, 2010). Although the analytic solutions provides accurate predictions of the electrostatic interactions in simple systems and help reveal the importance of the induced higher-order multipoles, it is generally difficult to directly apply these solutions to multiple-particle systems (Qin, de Pablo and Freed, 2016) as well as to non-spherical geometries.

To address this issue, different numerical methods have been developed and are becoming more promising with the growth of the computing power. To compute the electrostatic interaction between a collection of spheres, Lindgren, Stace, Polack, Maday, Stamm and Besley (2018a) presented the Galerkin approximation based on the truncated spherical harmonics series, which proved to be accurate and efficient. This approximation method was further employed in the dynamic simulations of the self-assembly and aggregation of charged dielectric spheres (Lindgren, Stamm, Maday, Besley and Stace, 2018b).

In addition, the finite element method (FEM) is also employed to compute the electrostatic interactions. The domain is generally discretized into regular elements on which the electrostatic problem is solved. Then the electrostatic interaction on each particle can be obtained by integrating over the surface elements. Compared to spherical harmonics, FEM can be applied to more complicated geometries, such as the multiple-particle case and non-spherical shapes. Feng (2000) first used FEM to calculate the electrostatic force between two touching dielectric spheres in a 2D domain. Recently, this method has been further extended to study the electrostatic attraction among up to tens of charged particles in a 3D domain (Matias, Shinbrot and Araújo, 2018).

If the geometry boundaries are sharp, the charge density reduces to the surface charge density, which significantly simplifies the electrostatic problem. Instead of discretizing the 3D domain, we only need to discretize the particle surfaces and calculate the surface charge distribution. Then the electrical field at a certain point can be obtained by summing the contribution over all the surface elements. This boundary element method (BEM) is of high efficiency and has been employed to simulate the self-assembly in colloids (Barros, Sinkovits and Luijten, 2014; Barros and Luijten, 2014).

Although BEM is applicable to complex geometries, present dynamic simulations mainly focus on charged dielectric spheres, and the more general non-spherical geometries have not been considered. Besides, for solid particles suspended in the gaseous flows or in the vacuum, the contact interactions between colliding particles may also play a crucial part in aggregation and triboelectrification (Güttler, Blum, Zsom, Ormel and Dullemond, 2010; Kline, Lim and Jaeger, 2020). Thus, a numerical model integrating both the electrostatic interaction and the contact interaction is of help to understand the underlying physics. In this study, we present a framework to conduct dynamic simulation of dielectric ellipsoidal particles carrying electrical charges. The surface charge density of dielectric particles is computed using the boundary element method. The electrostatic interaction is then calculated through surface integration. When interparticle collisions take place, the ellipsoids are treated as soft particles and the contact interactions are resolved based on the Hertzian theory. The electrostatic force between two dielectric spheres are first calculated using different models to show the impacts of the induced multipoles when particles are sufficiently close. Then the electrostatic force between two ellipsoids are given to show the influence of the non-spherical shape on the fundamental two-body interaction. Furthermore, the dynamic simulations of the particle-aggregate collision are performed with different post-collision outcomes, e.g., sticking, restructuring and fragmentation, to show the effect of the electrostatic interaction in the aggregation process.

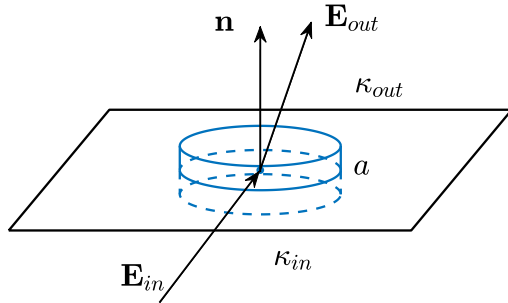


Figure 1: Schematic of the control volume on the particle surface. The outward unit vector points from the particle to the medium.

2. Methods

2.1. Electrostatic interactions between ellipsoids

2.1.1. Boundary element method

For dielectric particles, the external field could induce bound charge on the particle surface, which in turn affects the electrical field. The calculation of the electrical interactions thus becomes a coupled problem. In this study, the framework proposed by Barros et al. (2014); Barros and Luijten (2014) is employed to efficiently resolve the electrostatic interactions between dielectric particles. Here, we briefly derive the governing equation of the bound charge, and detailed information can be found in the references above.

In the vacuum, the electrical field \mathbf{E} is determined by the spatial charge density ρ as

$$\nabla \cdot \mathbf{E} = \rho/\epsilon_0 = (\rho_f + \rho_b)/\epsilon_0, \quad (1)$$

where ϵ_0 is the vacuum permittivity, ρ_f and ρ_b are the free and bound charge density. If the medium is linear, the polarization \mathbf{P} is proportional to the external field

$$\mathbf{P} = \epsilon_0(\kappa - 1)\mathbf{E}. \quad (2)$$

Here, κ is the dielectric constant of the medium. The polarization is also related to the bound charge density ρ_b by

$$\nabla \cdot \mathbf{P} = -\rho_b. \quad (3)$$

Combining Eqs 1, 2 and 3 then yield

$$\rho_f = \epsilon_0 \nabla \cdot (\kappa \mathbf{E}). \quad (4)$$

In this study, we focus on the electrostatic interactions between dielectric particles in the vacuum, so the dielectric constant only changes at the particle-vacuum interface. The charge density ρ then reduces to the surface charge density σ . To derive the governing equation of σ , we choose a flat cylinder as the control volume on the particle surface (shown in Fig 1). Integrating Eq 4 over the control volume

$$\int_V \rho_f dV = \int_V \epsilon_0 \nabla \cdot (\kappa \mathbf{E}) dV = \epsilon_0 \int_S \kappa \mathbf{E} \cdot \mathbf{n} dS \quad (5)$$

yields

$$\sigma_f(\mathbf{r}) = \epsilon_0 (\kappa_{out} \mathbf{E}_{out} - \kappa_{in} \mathbf{E}_{in}) \cdot \mathbf{n}. \quad (6)$$

Here, \mathbf{n} is the outward normal vector on the particle surface. By applying a similar process to Eq 1, we obtain

$$\sigma_f(\mathbf{r}) + \sigma_b(\mathbf{r}) = \epsilon_0(\mathbf{E}_{out} - \mathbf{E}_{in}) \cdot \mathbf{n}, \quad (7)$$

where $\sigma_f(\mathbf{r})$ and $\sigma_b(\mathbf{r})$ are the free and bound surface charge density. Taking Eq 6 into Eq 7, we obtain

$$\bar{\kappa}(\sigma_f + \sigma_b) + \epsilon_0 \Delta \kappa \mathbf{E} \cdot \mathbf{n} = \sigma_f, \quad (8)$$

where $\mathbf{E} = (\mathbf{E}_{out} + \mathbf{E}_{in})/2$ is the local field strength. $\bar{\kappa} = (\kappa_p + \kappa_0)/2$ is the average dielectric constant, and $\Delta \kappa = \kappa_0 - \kappa_p$ is the difference of the dielectric constants. After rearranging Eq 8, the governing equation of the bound charge is given by

$$\mathcal{A}\sigma_b = b \quad (9)$$

The left term of Eq 9 is

$$\mathcal{A}\sigma_b = \bar{\kappa}\sigma_b + \epsilon_0 \Delta \kappa \mathbf{E}_b \cdot \mathbf{n}, \quad (10)$$

while the right-hand-side term writes

$$b = (1 - \bar{\kappa})\sigma_f - \epsilon_0 \Delta \kappa \mathbf{E}_f \cdot \mathbf{n}. \quad (11)$$

$\mathbf{E}_b(\mathbf{r}_i)$ is the electrical field at \mathbf{r}_i induced by the bound charge on the surface, which reads

$$\mathbf{E}_b(\mathbf{r}_i) = \int_S \frac{\mathbf{r}_i - \mathbf{r}_j}{4\pi\epsilon_0 |\mathbf{r}_i - \mathbf{r}_j|^3} \sigma_b(\mathbf{r}_j) dS(\mathbf{r}_j). \quad (12)$$

\mathbf{E}_f is the electric field induced by the free charge that can be obtained similar to Eq 12. In the simulation, the free charge σ_f is assumed to be uniformly distributed on the surface, and Eq 9 is solved to obtain the bound charge density σ_b . The electrostatic force \mathbf{F}_E and torque \mathbf{M}_E can then be computed by integrating the force and torque over the surface of each particle

$$\mathbf{F}_E = \int_S \kappa_0(\sigma_f + \sigma_b) \mathbf{E} dS, \quad (13a)$$

$$\mathbf{M}_E = \int_S \kappa_0(\sigma_f + \sigma_b) \mathbf{r} \times \mathbf{E} dS. \quad (13b)$$

2.1.2. Surface discretization

To implement Eq 9, the ellipsoidal surface is discretized into triangular surface patches using the open-source code *DistMesh* developed by Persson and Strang (2004). During mesh generation, the vertices adjust their positions dynamically under the repulsive force exerted by other adjacent vertices. When the equilibrium is reached, the vertices become nearly equidistant (shown in Fig 2). Then the matrix in Eq 9 can be discretized as

$$\mathcal{A}_{ij} = \bar{\kappa}_i \delta_{ij} + \Delta \kappa_i \mathbf{n}_i \cdot \mathbf{I}_{ij} a_j \quad (14)$$

where the components of \mathbf{I}_{ij} is the Green function from the j th patch to the i th patch that is given by

$$\mathbf{I}_{ij} = (\mathbf{r}_i - \mathbf{r}_j) / 4\pi |\mathbf{r}_i - \mathbf{r}_j|^3 \quad (15)$$

The Green function becomes singular when considering the contribution of each patch to itself (\mathbf{I}_{ii}). In the present study, this self contribution is omitted by

$$\mathbf{I}_{ii} = \mathbf{0}. \quad (16)$$

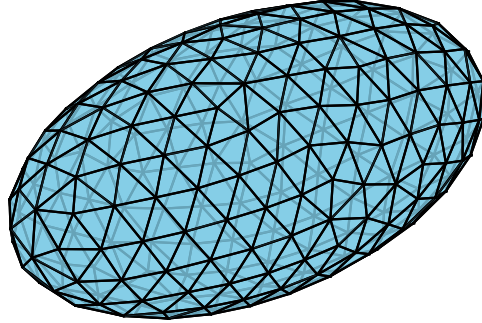


Figure 2: Schematic of the triangular surface patches

2.1.3. GMRES-FMM coupled calculation

As suggested by Barros et al. (2014), instead of directly calculating the inverse matrix A^{-1} , the method of generalized minimum residual (GMRES) is used to solve Eq 9. In the m th iteration, the m th-order Krylov subspace is generated as

$$K_m = \text{span}\{\mathbf{b}, \mathcal{A}\mathbf{b}, \dots, \mathcal{A}^{m-1}\mathbf{b}\}. \quad (17)$$

Then the approximated solution $\sigma_b^{(m)}$ is obtained in K_m by solving the least square problem

$$\min \|\mathbf{r}^{(m)}\| = \min \|\mathbf{b} - \mathcal{A}\sigma_b^{(m)}\|. \quad (18)$$

Since $K_m \supset K_{m-1}$, the residual will decrease monotonically as $\|\mathbf{r}^{(m)}\| \leq \|\mathbf{r}^{(m-1)}\|$. When the relative tolerance is smaller than the preset criterion

$$\frac{\|\mathbf{r}^{(m)}\|}{\|\mathbf{b}\|} < 10^{-4}, \quad (19)$$

the solution converges. The most expensive section in the m th iteration is to calculate the matrix-vector product $\mathcal{A}^{m-1}\mathbf{b} = \mathcal{A} \times \mathcal{A}^{m-2}\mathbf{b}$ in Eq 17, which scales as $O(n^2)$ with n being the dimension of \mathcal{A} , or the total number of surface patches in the system. As the particle number becomes larger or a finer mesh is employed, the calculation becomes more expensive. Since the matrix-vector product can be treated as a direct electrostatic problem according to Eq 10, the fast multipole method (FMM) can be implemented to accelerate the calculation (Greengard and Rokhlin, 1987).

The present code is written in MATLAB and run on a typical desktop with Intel(R) Core(TM) i7-8700 CPU at 3.20 GHz and 16.0GB RAM. In GMRES implementation, the library *FMMLIB3D* by Greengard and Gimbutas (github.com/zgimbutas/fmmlib3d) is called to conduct the fast matrix-vector product. To compare the calculation cost, we measure the CPU time required to calculate the electrostatic problem in static cases with different number of particles and surface patches. In each case, ten individual runs are performed to obtain the average CPU time. The standard deviations are shown as the error bars. Fig 3(a) plots the average CPU times of each GMRES iteration with a group of particles arranged in a row. The surface patch number of each particles is fixed as 392, and the surface-to-surface distance between adjacent particles is $d = 0.2R$. A quadratic dependence of CPU time on particle number is observed when only using GMRES, while the CPU time scales as $n^{1.333}$ if FMM is employed. 3(b) shows the calculation cost between two spheres with the surface-to-surface distance $d = 0.5R$. The quadratic scaling is also found without FMM. When FMM is incorporated, the cost scales as $n^{1.564}$ when the number of surface patches on each particle increases. Thus, the calculation cost is significantly reduced with the naive implementation of FMM in

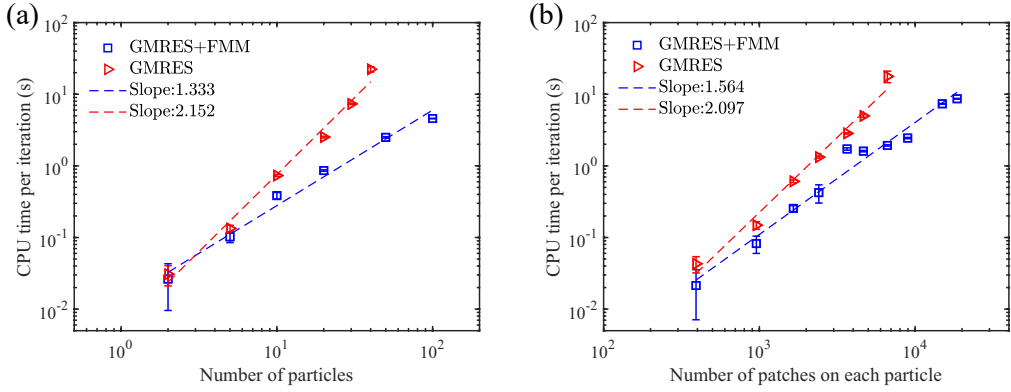


Figure 3: Dependence of CPU time of every GMRES iteration on (a) the number of particles and (b) the number of surface patches.

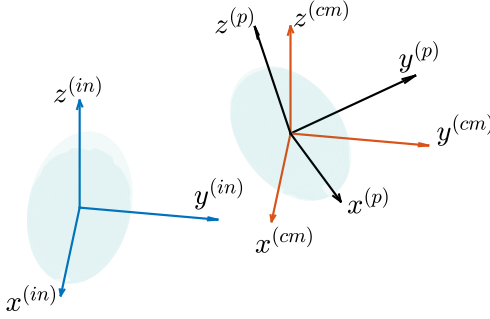


Figure 4: Schematic of different coordinate frames. The inertial, co-moving and particle frames are colored in blue, red and black.

the present study. For a more sophisticated implementation of FMM that optimizes the octree structure, a linear or nearly linear growth of the calculation cost can be expected (Barros et al., 2014; Lindgren et al., 2018a).

Apart from the calculation efficiency, the accuracy of our BEM has been validated through extensive simulations. In Appendix A, the electrical energy between a point charge and a neutral dielectric sphere is shown and compared with the theoretical solution.

2.2. Particle Transport

Three coordinate frames are used to describe the position and orientation of ellipsoidal particles, which can be referred to as the inertial frame $\mathbf{x}^{(in)} = [x^{(in)}, y^{(in)}, z^{(in)}]^T$, the co-moving frame $\mathbf{x}^{(cm)} = [x^{(cm)}, y^{(cm)}, z^{(cm)}]^T$ and the particle frame $\mathbf{x}^{(p)} = [x^{(p)}, y^{(p)}, z^{(p)}]^T$ (shown in Fig 4). The co-moving frame translates with the particle and its origin is fixed at the particle centroid. The axes of the particle frame always coincide with the semi-axes of the ellipsoid, so the particle frame records both the translational and rotational movements of the particle. Transformation between different frames are given in Appendix B.

The discrete element method (DEM) is employed to evolve particle movements. The governing equations of the linear and angular momentum are given as

$$m \frac{d\mathbf{v}_i^{(in)}}{dt} = \mathbf{F}_{E,i}^{(in)} + \sum_{j \neq i} \mathbf{F}_{C,j \rightarrow i}^{(in)}, \quad (20)$$

$$I_x^{(p)} \frac{d\Omega_{x,i}^{(p)}}{dt} - \Omega_{y,i}^{(p)} \Omega_{z,i}^{(p)} (I_y^{(p)} - I_z^{(p)}) = M_{E,i,x}^{(p)} + \sum_{j \neq i} M_{C,j \rightarrow i,x}^{(p)}, \quad (21a)$$

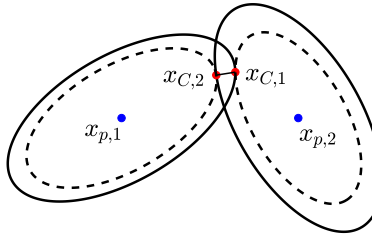


Figure 5: Schematic of collision detection.

$$I_y^{(p)} \frac{d\Omega_{y,i}^{(p)}}{dt} - \Omega_{z,i}^{(p)} \Omega_{x,i}^{(p)} (I_z^{(p)} - I_x^{(p)}) = M_{E,i,y}^{(p)} + \sum_{j \neq i} M_{C,j \rightarrow i,y}^{(p)}, \quad (21b)$$

$$I_z^{(p)} \frac{d\Omega_{z,i}^{(p)}}{dt} - \Omega_{x,i}^{(p)} \Omega_{y,i}^{(p)} (I_x^{(p)} - I_y^{(p)}) = M_{E,i,z}^{(p)} + \sum_{j \neq i} M_{C,j \rightarrow i,z}^{(p)}. \quad (21c)$$

Here, $\mathbf{v}_i^{(in)}$ and $\boldsymbol{\Omega}_i^{(p)} = [\Omega_{x,i}^{(p)}, \Omega_{y,i}^{(p)}, \Omega_{z,i}^{(p)}]^T$ are the velocity and the rotation rate of particle i . m is the particle mass, $\mathbf{I}^{(p)} = [I_x^{(p)}, I_y^{(p)}, I_z^{(p)}]^T$ is the moment of inertia with $I_x^{(p)} = m(b^2 + c^2)/5$, $I_y^{(p)} = m(c^2 + a^2)/5$ and $I_z^{(p)} = m(a^2 + b^2)/5$. $\mathbf{F}_{E,i}^{(in)}$ and $\mathbf{M}_{E,i}^{(in)}$ are the electrostatic force and torque exerted on particle i . $\mathbf{F}_{C,j \rightarrow i}^{(in)}$ and $\mathbf{M}_{C,j \rightarrow i}^{(p)} = [M_{C,j \rightarrow i,x}^{(p)}, M_{C,j \rightarrow i,y}^{(p)}, M_{C,j \rightarrow i,z}^{(p)}]^T$ are the contact force and torque acting on particle i by particle j .

When two particles are detected to collide, the contact points are determined using the method of level surfaces shown in Fig 5 (see Appendix C for details). The velocity at the contact point is then given by

$$\mathbf{v}_{C,i}^{(in)} = \mathbf{v}_i^{(in)} + \boldsymbol{\Omega}_i^{(in)} \times \mathbf{r}_{C,i}^{(in)}, \quad (22)$$

where $\mathbf{r}_{C,i}^{(in)} = \mathbf{x}_{C,i}^{(in)} - \mathbf{x}_{p,i}^{(in)}$ points from the ellipsoid centroid to the contact point. The normal velocity $\mathbf{v}_{rel,n}^{(in)}$ and the tangential velocity $\mathbf{v}_{rel,t}^{(in)}$ are defined by

$$\mathbf{v}_{rel,n}^{(in)} = (\mathbf{v}_{C,i}^{(in)} - \mathbf{v}_{C,j}^{(in)}) \cdot \mathbf{n}, \quad (23)$$

and

$$\mathbf{v}_{rel,t}^{(in)} = (\mathbf{v}_{C,i}^{(in)} - \mathbf{v}_{C,j}^{(in)}) - (\mathbf{v}_{C,i}^{(in)} - \mathbf{v}_{C,j}^{(in)}) \cdot \mathbf{n}. \quad (24)$$

Here, the unit vector along the outward normal direction at the contact point are given by

$$\mathbf{n}(\mathbf{x}_{C,i}^{(in)}) = \nabla P_i(\mathbf{x}_{C,i}^{(in)}) / \left| \nabla P_i(\mathbf{x}_{C,i}^{(in)}) \right|, \quad (25)$$

while the tangent unit vector equals

$$\mathbf{t} = \mathbf{v}_{rel,t}^{(in)} / |\mathbf{v}_{rel,t}^{(in)}|. \quad (26)$$

In each collision, particles are treated as soft spheres. The contact force $\mathbf{F}_{C,j \rightarrow i}^{(in)}$ and torque $\mathbf{M}_{C,j \rightarrow i}^{(in)}$ are calculated according to the Hertz contact model (Marshall, 2009).

$$\mathbf{F}_{C,j \rightarrow i}^{(in)} = (F_{ne} + F_{nd})\mathbf{n} + F_t\mathbf{t} \quad (27)$$

Here, the normal force consists of two terms, i.e., the normal elastic force F_{ne} and the normal dissipation force F_{nd} . The normal elastic force can be expressed as

$$F_{ne} = -k_N \delta_N, \quad (28)$$

with $\delta_N = |\mathbf{x}_{C,i}^{(in)} - \mathbf{x}_{C,j}^{(in)}|$ being the normal overlap. The elastic stiffness k_N is written as

$$k_N = \frac{4}{3} E \sqrt{R \delta_N}, \quad (29)$$

The effective radius R is defined by the mean curvature of two ellipsoids at their contact points as

$$R = (K_{C,i} + K_{C,j})^{-1}, \quad (30)$$

with the local mean curvature K_i given by

$$K_i = \frac{h^3}{2} \left[\frac{1}{a^2 b^2} \left(\frac{(x_i^{(p)})^2}{a^2} + \frac{(y_i^{(p)})^2}{b^2} \right) + \frac{1}{b^2 c^2} \left(\frac{(y_i^{(p)})^2}{b^2} + \frac{(z_i^{(p)})^2}{c^2} \right) + \frac{1}{c^2 a^2} \left(\frac{(z_i^{(p)})^2}{c^2} + \frac{(x_i^{(p)})^2}{a^2} \right) \right], \quad (31a)$$

$$h = [(x_i^{(p)})^2/a^4 + (y_i^{(p)})^2/b^4 + (z_i^{(p)})^2/c^4]^{-1/2}. \quad (31b)$$

The effective elastic modulus E is defined as

$$\frac{1}{E} = \frac{1 - \nu_i^2}{E_i} + \frac{1 - \nu_j^2}{E_j}, \quad (32)$$

where E_i and ν_i are the elastic modulus and Poisson ratio of particle i . The normal dissipation force is proportional to the normal relative velocity

$$F_{nd} = -\eta_N \mathbf{v}_{rel} \cdot \mathbf{n}, \quad (33)$$

where the normal dissipation coefficient is defined as

$$\eta_N = \alpha_N (m k_N)^{1/2}. \quad (34)$$

Here, m is the particle mass, α_N is related to the coefficient of restitution e (Marshall, 2009). The tangential force is calculated based on the static friction model and written as

$$F_t = -\mu_F |F_n| \quad (35)$$

where $\mu_F = 0.3$ is the friction coefficient. Once the full contact force $\mathbf{F}_{C,j \rightarrow i}^{(in)}$ is obtained, the corresponding rotation torque is computed by

$$\mathbf{M}_{C,j \rightarrow i}^{(in)} = \mathbf{r}_{C,ij}^{(in)} \times \mathbf{F}_{C,j \rightarrow i}^{(in)}. \quad (36)$$

3. Results and Discussions

3.1. Electrostatic force between charged spheres

To evaluate the applicability of different electrostatic models, we compute the electrostatic force between two dielectric spheres using the point charge model, the induced dipole model and BEM. By comparing the results, it is of interest to figure out in what regime can the fundamental particle-particle interaction be captured by the simplified point charge model and the induced dipole model.

In the induced dipole model, the electrical dipole moment \mathbf{p} describes the polarization of the dielectric particle. The electrostatic force acting on particle i located at \mathbf{x}_i is given by

$$\mathbf{F}_{E,i} = q_i \mathbf{E}(\mathbf{x}_i) + \mathbf{p}_i \cdot \nabla \mathbf{E}(\mathbf{x}_i), \quad (37)$$

where q_i is the net charge on the particle, \mathbf{p}_i is the dipole moment. The electric field at the particle position is

$$\mathbf{E}(\mathbf{x}_i) = \sum_{j \neq i} \left[\frac{q_j \mathbf{r}_{ij}}{4\pi\epsilon_0 r_{ij}^3} - \nabla \left(\frac{\mathbf{p}_j \cdot \mathbf{r}_{ij}}{4\pi\epsilon_0 r_{ij}^3} \right) \right]. \quad (38)$$

Here, the induced dipole is assumed to depend linearly on the local field strength as

$$\mathbf{p}_i = 4\pi\epsilon_0 K_{CM} r_p^3 \mathbf{E}(\mathbf{x}_i), \quad (39)$$

where the *Clausius-Mossotti* function K_{CM} equals

$$K_{CM} = \frac{\kappa_p - \kappa_0}{\kappa_p + 2\kappa_0}. \quad (40)$$

To solve the coupled problem given by Eq 38 and Eq 39, we assume the initial dipole $\mathbf{p}_i^{(0)} = \mathbf{0}$ and compute the field strength $\mathbf{E}^{(0)}(\mathbf{x}_i)$. Eq 38 and Eq 39 are iterated until \mathbf{p}_i converges. Then the electrostatic force is obtained from Eq 37.

Fig 6(a) plots the normalized electrostatic force F/F_0 between two identically charged dielectric spheres with the dimensionless surface-to-surface distance d/R . For simplicity, the nominal surface charge density is $\sigma_f = 1$. $F_0 = q_0^2/[4\pi\epsilon_0(2R)^2]$ is the characteristic Coulomb force with $q_0 = 4\pi R^2 \sigma_f$ being the net charge on the sphere. As shown in Fig 6(a), the curve of $\kappa_p = 1$ coincides with that predicted by the point charge model. This means if the effect of the induced surface charge is neglected, the electrostatic interaction will reduce to the simple Coulomb interaction. When the spheres become polarizable ($\kappa_p > 1$), the bound charge σ_b is induced as two spheres approach each other. The resulting repulsive force is weakened and deviates from the Coulomb force when $d/R \leq 2$. To better illustrate this change, the typical charge distribution is displayed in Fig 6(b). When two equally charged spheres get close, bound charge of the opposite sign will be induced on the near side, while the same-sign charge will be induced on the far side. Although the net charge on each sphere is conserved, the near-side charge that has a major contribution to the electrostatic force is partially neutralized, which results in the decrease of the overall electrostatic force. In addition, the effect of particle polarization is found to saturate when κ_p is large (e.g., $\kappa = 40$ and $\kappa_p = 100$ in Fig 6(b)). Further increasing κ_p does not weaken the repulsive force to a larger extent.

The electrostatic force predicted by the induced dipole model is also shown as the dark blue dash line in Fig 6(a). In the dipole model, the polarization of the particle can be approximated by the relative shift of the positive and negative charge at the particle scale. For two equally charged dielectric spheres shown in Fig 6(b), there is obvious particle-scale separation between the positive and negative surface charge, which satisfies the above assumption. Thus, the induced dipole model could well predict the electrostatic force despite its simplified nature. Besides, when κ_p is sufficiently large, the Clausius-Mossotti function K_{CM} approaches unity, which explains the saturation of F/F_0 when κ_p further increases.

Nevertheless, the dipole model underestimates the enhanced attractive force between two oppositely charged spheres when they are sufficiently close. For two dielectric spheres carrying the opposite charges, the bound charge density

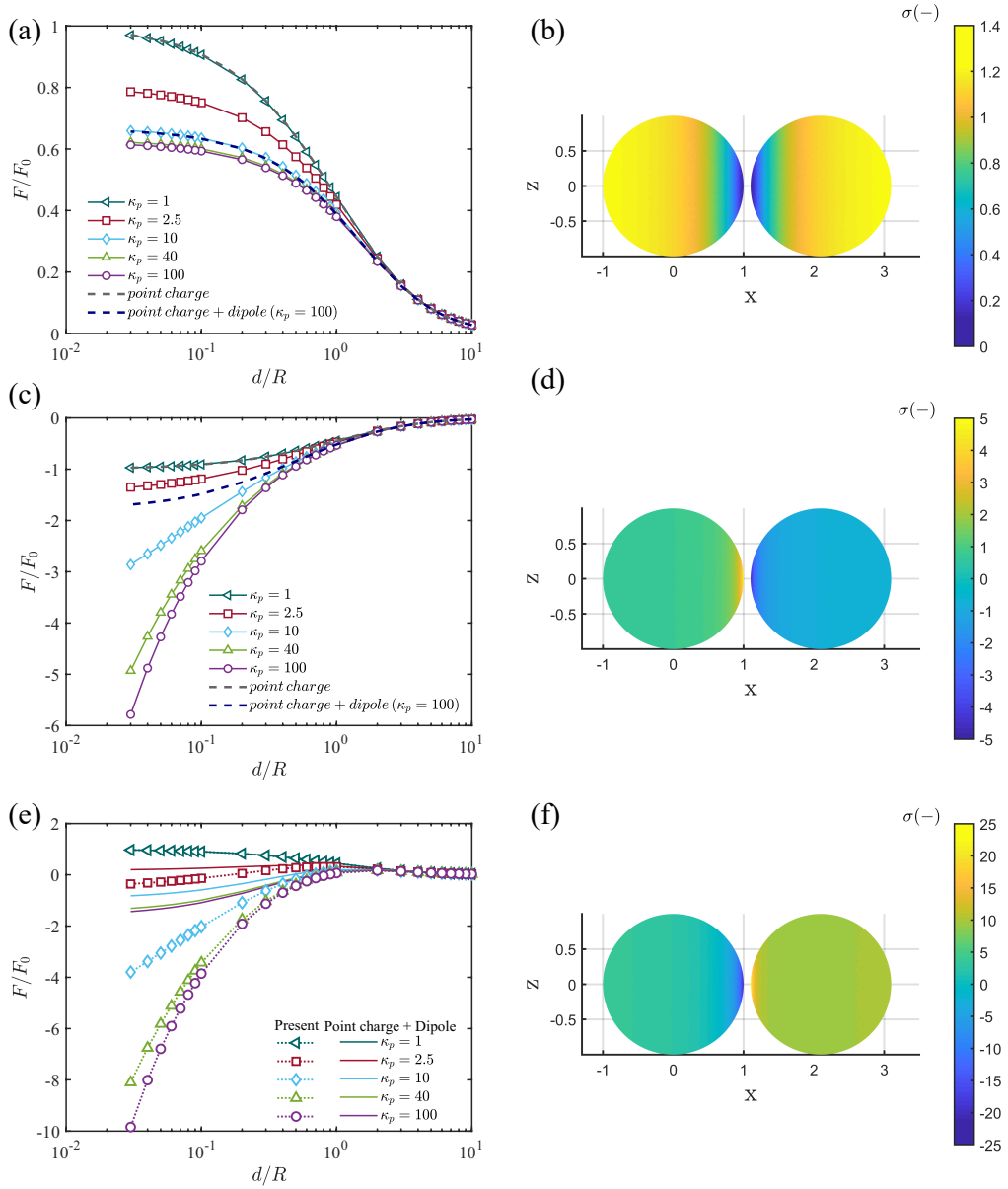


Figure 6: Dependence of the normalized electrostatic force F/F_0 on the normalized surface-to-surface separation distance d/R between two dielectric particles with the nominal charge density (a) $\sigma_{f,1} = \sigma_{f,2} = 1$, (c) $\sigma_{f,1} = 1, \sigma_{f,2} = -1$ and (e) $\sigma_{f,1} = 1, \sigma_{f,2} = 10$. (b), (d), (f): The surface charge distribution of two close particles with $\kappa_p = 10$ and $d/R = 0.1$ corresponding to (a), (c) and (e)

becomes higher on the near side of each particle because of the electrostatic attraction by the other particle. The induced charge will in return enhances this attraction. As a result, the local charge density becomes much higher than the initial free charge density and thus drastically increases the attractive force between two spheres (Fig 6(c)). However, the induced charge is only dominant in a small region on the near side as shown in Fig 6(d), which is beyond the description of the dipole model. As a result, the dipole model significantly underestimates the electrostatic attraction between two spheres (dark blue dash line in 6(c)).

Apart from spheres carrying equal amount of charges, it is interesting to also investigate the electrostatic force between spheres carrying different amount of surface charges. Fig 6(e) plots the dependence of F/F_0 on d/R between two positively charged spheres. The nominal charge density are $\sigma_1 = 1$ (left) and $\sigma_2 = 10$ (right) shown in Fig 6(f).

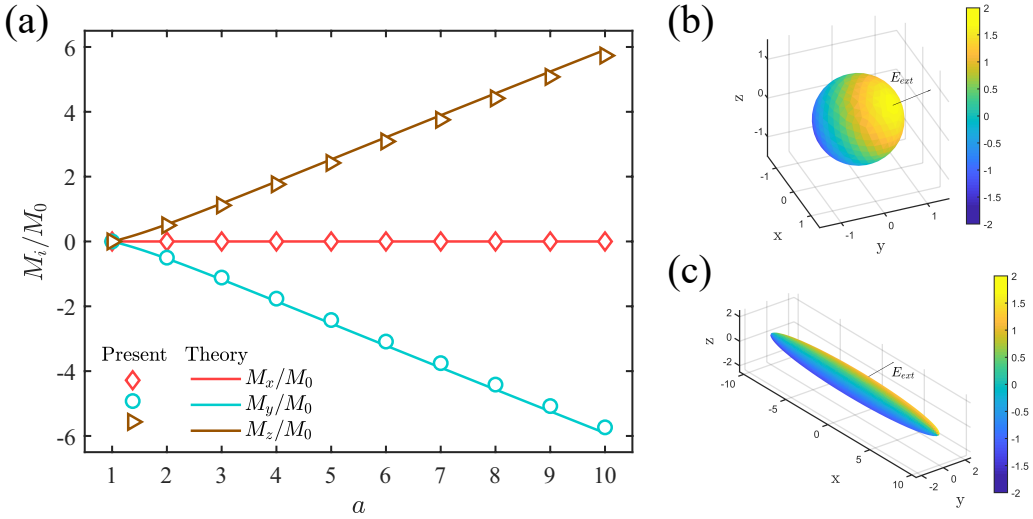


Figure 7: (a) Normalized torque acting on the dielectric ellipsoid exerted by the external field. Distribution of the nominal surface charge density for (b) $a = 1$ and (c) $a = 10$ under the external field.

a	1	2	3	4	5	6	7	8	9	10
N_{patch}	956	1564	2204	2812	3516	4092	4732	5340	6012	6556

Table 1

Number of surface patches N_{patch} for different semi-axis lengths a .

The characteristic force $F_0 = \pi R^2 \sigma_1 \sigma_2 / \epsilon_0$. The electrostatic force is always repulsive if the induced charge is omitted ($\kappa_p = 1$). However, when the spheres becomes polarized, due to the obvious difference of the net charge, negative charge will be induced on the near side of the left particle, which triggers the self-enhancing process introduced above. Consequently, the local charge density increases drastically as two spheres get close. F/F_0 even becomes attractive when they are close enough, which is consistent with previous studies by Feng (2000); Matias et al. (2018). Again, since the dipole model cannot capture the local charge distribution on the near side, the attractive force at a small separation is underestimated. In such cases, higher-order multipoles should be resolved to well predict the strong but local effect of induced charge.

3.2. Electrostatic interaction on non-spherical particles

Different from the spherical geometry, the electrostatic interaction acting on non-spherical particles is orientational even though the dielectric property of particle material is homogeneous and isotropic. In this section, we focus on the modulation of the electrostatic interaction caused by the geometrical anisotropy of non-spherical particles.

3.2.1. Electrostatic torque on an ellipsoidal particle

If a neutral dielectric ellipsoid is placed in a uniform external field, the net electrostatic force remains zero since the net charge on the ellipsoid remains zero. However, the surface charge distribution could become asymmetric due to the non-spherical shape, which leads to a non-zero electrostatic torque acting on the ellipsoid. For a neutral dielectric ellipsoid defined by $x^2/a^2 + y^2/b^2 + z^2/c^2 = 1$, the electrostatic torque \mathbf{M}_E exerted by the external field $\mathbf{E}_{ext} = [E_x, E_y, E_z]$ is given by (Jones, 1995)

$$M_{E,x} = \frac{4\pi\epsilon_m abc}{3} \cdot \frac{(\tilde{\kappa} - 1)^2 (L_z - L_y) E_z E_y}{[1 + (\tilde{\kappa} - 1)L_z][(\tilde{\kappa} - 1)L_y]}, \quad (41a)$$

$$M_{E,y} = \frac{4\pi\epsilon_m abc}{3} \cdot \frac{(\tilde{\kappa} - 1)^2(L_x - L_z)E_x E_z}{[1 + (\tilde{\kappa} - 1)L_x][(\tilde{\kappa} - 1)L_z]}, \quad (41b)$$

$$M_{E,z} = \frac{4\pi\epsilon_m abc}{3} \cdot \frac{(\tilde{\kappa} - 1)^2(L_y - L_x)E_y E_x}{[1 + (\tilde{\kappa} - 1)L_y][(\tilde{\kappa} - 1)L_x]}. \quad (41c)$$

Here, κ_m is the dielectric constant of the medium, $\tilde{\kappa} = \kappa_p/\kappa_m$ is the ratio of the dielectric constants. The elliptical integrals are defined as

$$L_x = \frac{abc}{2} \int_0^\infty \frac{ds}{(s + a^2)R_s}, \quad (42a)$$

$$L_y = \frac{abc}{2} \int_0^\infty \frac{ds}{(s + b^2)R_s}, \quad (42b)$$

$$L_z = \frac{abc}{2} \int_0^\infty \frac{ds}{(s + c^2)R_s}, \quad (42c)$$

with $R_s = [(s + a^2)(s + b^2)(s + c^2)]^{1/2}$.

For simplicity, the parameters are set dimensionless here. We consider a spheroid under an external field $\mathbf{E} = E_0[1, 1, 1]$. The dielectric constant of the particle and the medium is $\kappa_p = 2.5$ and $\kappa_m = 1$. The minor semi-axis lengths are fixed as $b = c = 1$ while the major semi-axis length a ranges from 1 to 10. Fig 7(a) compares the electrostatic torque given by Eq 41 and normalized by $M_0 = 4\pi\epsilon_m R_0^3 E_0^2 / 3$. The BEM markers collapse on to the theoretical curves in Fig 41(a), which proves the applicability of the present method on ellipsoidal geometries. Table 1 lists the number of surface patches for different semi-axis lengths a . As a increases, more patches are required to well discretize the ellipsoidal surface.

When $a = 1$, the ellipsoid reduces to a sphere, and the electrostatic torque is zero. This is because the induced charge on the sphere is symmetric about the direction of the external field (Fig 7(b)). When summing over the whole spherical surface, the torque exerted on each patch will cancel out. However, as the ellipsoid elongates, the induced charge on the ellipsoidal surface is not axisymmetric about the external field any more (Fig 7(c)). Integrating over the ellipsoidal surface then yields a non-zero net torque. The effect of this torque is to rotate the ellipsoid in a way that the asymmetry of the surface charge can be eliminated. Consequently, when the ellipsoid aligns its major axis in the direction of the field strength \mathbf{E} , the electrostatic torque becomes zero.

3.2.2. Electrostatic force between two charge dielectric ellipsoids

For spherical particles discussed in Section 3.1, the electrostatic force does not rely on the direction along which two particles approach each other. But for ellipsoidal particles, the particle orientation affects the system geometry and modifies the electrostatic force. Thus, it is of help to study the two-body electrostatic force between two ellipsoids.

Without loss of generality, three typical configurations are chosen here, i.e., two particles approach each other (i) both along the major axis (head-to-tail configuration in Fig 8(b)), (ii) along the major and minor axis respectively (perpendicular configuration in Fig 8(c)) and (iii) both along the minor axis (side-by-side configuration in Fig 8(d)). Here, the dielectric constant is $\kappa_p = 10$ and the dimensionless charge density is $\sigma_f = \pm 1$. The semi-axis lengths are $a = 2$ and $b = c = 1$.

Fig 8(a) compares the dependence of the normalized electrostatic force F/F_0 on the surface-to-surface distance d/c between three different configurations. The characteristic force is $F_0 = \pi c^2 \sigma_f^2 / \epsilon_m$. It can be found that as two ellipsoids get close, the induced charge will mitigate the repulsion between identically charged particles while enhance the attraction between oppositely charged particles, which is similar to that observed in the spherical case.

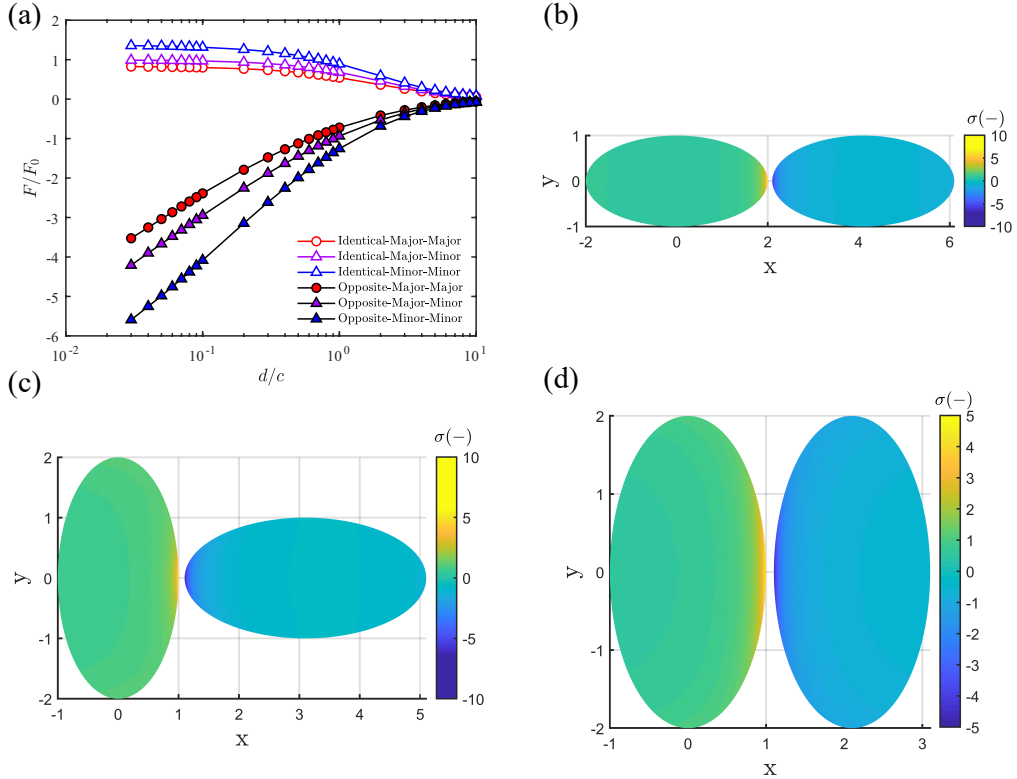


Figure 8: The normalized electrostatic force F/F_0 between two dielectric ellipsoids with the nominal charge density $\sigma_{f,1} = 1$ and $\sigma_{f,2} = -1$. The nominal surface charge distribution of two ellipsoids approaching each other (a) both along the major axis, (b) along the major and minor axis respectively and (c) both along the minor axis with $\kappa_p = 10$ and $d/R = 0.1$.

By comparing the force between different configurations, the strongest force appears when two ellipsoids arrange in the side-by-side configuration, while the weakest force is noticed in the head-to-tail configuration. This can be attributed to the short-range nature of the induced higher-order multipoles. Although the higher-order multipoles are very strong when particles are in close contact, their magnitudes decay rapidly as the surface-to-surface distance increases. In the head-to-tail configuration (Fig 8(b)), the high charge density is observed within a small region at the near-side tips. Since the local curvature is large, as we move from the tip to the outer region, the distance between two surfaces increases quickly, which causes the rapid decrease of the charge density. Consequently, the impact of the induced higher-order multipoles is limited. In contrast, in the side-by-side configuration shown in Fig 8(d), even though the charge density becomes lower compared to the head-to-tail configuration, a much larger region is in close contact due to the small local curvature. As a result, the contribution of all the induced surface charge is more significant and lead to a stronger electrostatic force. For the perpendicular configuration plotted in Fig 8(c), the close contacting area is in the middle compared to other two configurations, so a moderate force is reported in Fig 8(a). Based on the conclusion here, different configurations can be expected in the dynamic processes of particle aggregation or assembly. When forming an aggregate, particles need to adjust their position and orientation continuously to minimize the system energy. For identically charged particles, particles might organize in the head-to-tail configuration so that they feel less repulsion. And the side-by-side configuration may be favored between oppositely charged particles because of the stronger attraction as they both approach along the minor axis.

3.3. Dynamic simulation of particle-aggregate collision

In dynamic simulations, the surface patches *cannot* coincide. If two surface patches i and j coincide, the corresponding Green function \mathcal{I}_{ij} defined in Eq 15 becomes singular. However, the overlap between two surfaces is required to detect collision and compute the contact interactions (Appendix C). In this study, we use the *double-shell model* to address this problem. As shown in Fig 9(a), two different shells are used to calculate the electrostatic interaction and

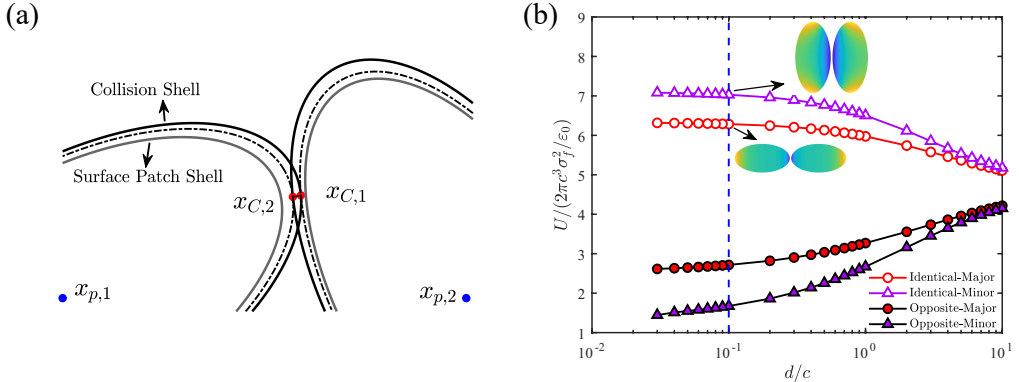


Figure 9: (a) Schematic of the double-shell model. The collision shell is plotted as black profiles and the surface patch shell is shown as grey profiles. The level surfaces are denoted by the dash dot lines. (b) Dimensionless electrostatic energy between two ellipsoids with $\kappa_p = 10$.

the contact interaction, respectively. The original ellipsoidal surface is the surface patch shell (grey profile) on which the discretized surface patches locate, while a slightly larger surface is used to calculate the contact interactions (black profile). The thickness of the *buffer layer* between these two shells is defined as δ_{bl} . The characteristic matrix of the ellipsoid i in Eq 53 then becomes

$$\mathcal{Q}_i^{(p)} = \begin{bmatrix} 1/(a + \delta_{bl})^2 & 0 & 0 & 0 \\ 0 & 1/(b + \delta_{bl})^2 & 0 & 0 \\ 0 & 0 & 1/(c + \delta_{bl})^2 & 0 \\ 0 & 0 & 0 & -1 \end{bmatrix}. \quad (43)$$

As shown in Fig 17, the maximum overlap $\delta_{N,max}$ is generally small compared to the particle size ($\delta_{N,max}/R \lesssim 1\%$), so the value of δ_{bl} can be set small to reduce the relative error introduced by the double-shell model.

$$U = \frac{1}{2} \int_S \sigma_f(\mathbf{r}) \psi(\mathbf{r}) dS \quad (44)$$

Fig 9(b) plots the normalized electrostatic energy calculated by Eq 44 as a function of the normalized surface-to-surface separation d/c . Here, the particle dielectric constant $\kappa_p = 10$ is comparable to that reported by Lee et al. (2015). As two ellipsoids approach each other along the direction of the major/minor semi-axis, the corresponding energies are given as red/purple markers. It is found that the electric energy almost saturates when the surface-to-surface distance satisfies $d \leq 0.1c$ (vertical blue line in Fig 9(b)). The thickness of the buffer layer is thus chosen as $\delta_{bl} = 0.05 \times \min\{a, b, c\}$ in the dynamic simulations.

In this section, we simulate the collision process between a neutral ellipsoidal particle and an aggregate formed by two oppositely charged ellipsoids. Different collision outcomes, such as sticking, restructuring and fragmentation, are reproduced to show the influence of the electrostatic interactions on particle aggregation. The simulation parameters are listed in Table 2. The reduced elastic modulus E_R is used to accelerate the calculation (see Appendix D).

Fig 10 shows the snapshots of a typical collide-and-stick process. The initial configuration is displayed in Fig 10(a). Particle 1 and 2 are at rest and stick together side-by-side, while the incident particle 3 moves towards the aggregate with an initial velocity $v_{in} = 0.02 \text{ m/s}$. Due to the induced surface charges, the electrostatic force acting on particle 3 becomes attractive when it is sufficiently close to the aggregate, which accounts for the acceleration of the incident particle (Fig 11(a)) and the decrease of the electrostatic energy (Fig 11(c)). When the first collision occurs, part of the kinetic energy is transferred to the aggregate, so the aggregate starts to translate along the x direction ($t \sim 1.1 \text{ ms}$ in Fig 11(a)). Meanwhile, particle 1 and 2 begin to separate by rotating along opposite directions. During the separation, particles need to overcome the electrostatic attraction by decreasing their kinetic energy, which leads to the increase of U between point b and c in 11(c)). In this case, since the kinetic energy is not large enough for particles to escape, particle 1 and 2 fall back and collide again. As the restitution coefficient is smaller than unity, the kinetic energy is

Parameters	Values	Units
Particle size, $a/b/c$	100/50/50	μm
Buffer layer thickness, δ_{bl}	2.5	μm
Particle density, ρ_p	2500	kg/m^3
Free charge density, σ_f	± 5	$\mu\text{C}/\text{m}^2$
Original elastic modulus, E_0	1×10^9	Pa
Reduced ratio, χ	5.52×10^{-3}	—
Reduced elastic modulus, E_R	5.52×10^6	Pa
Dielectric constant of particle, κ_p	10	—
Dielectric constant of medium, κ_m	1	—
Restitution coefficient, e	0.7	—
Friction coefficient, μ_F	0.3	—
Incident velocity, v_{in}	0.02/0.16	m/s

Table 2

Simulation parameters of the particle-aggregate collision.

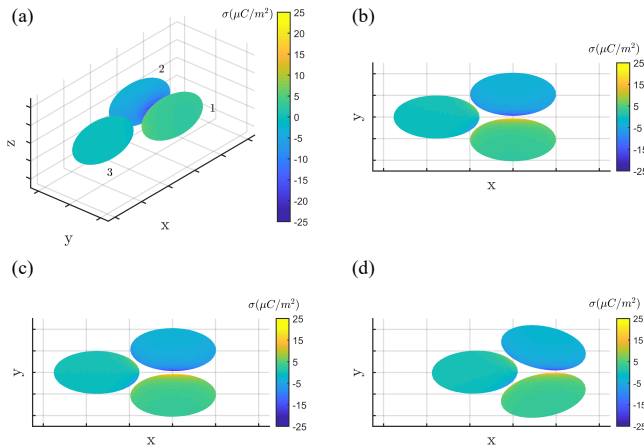


Figure 10: Snapshots of the collision process between ellipsoid 3 and the side-by-side aggregate formed by ellipsoids 1 and 2 at (a) $t = 0.03 \text{ ms}$, (b) $t = 1.11 \text{ ms}$, (c) $t = 1.29 \text{ ms}$ and (d) $t = 9.6 \text{ ms}$. The incident velocity of ellipsoid 3 is $v_{in} = 0.02 \text{ m/s}$ along the x direction.

effectively damped after each collision. Eventually, when all the relative kinetic energy is dissipated, three primary particles stabilize at a new state and move as a whole (10(d)). The interparticle overlaps in this state are determined by the balance between the electrostatic attraction and the elastic repulsion (shown in the inset of 11(b)).

Fig 12 shows the snapshots of a collision-induced fragmentation process. The initial configuration is the same as shown in Fig 10(a) except for a large incident velocity $v_{in} = 0.16 \text{ m/s}$. After the first collision, the primary particles contained in the aggregate obtain a larger translation velocity (Fig 13(a)) and moves forward. At the same time, particle 1 and 2 also separate with a high rotate rate. After encountering the second collision at $t = 1.2 \text{ ms}$ (Fig 13(b)), the rebound velocity is large enough for particle 1 and 2 to bounce away. In this process, the relative kinetic energy is stored in the form of the electrostatic energy shown as Fig 13(c). Therefore, if primary particles could obtain sufficient kinetic energy to overcome the binding energy between charged particles, the collision will eventually lead to fragmentation.

Collision-induced restructuring is observed when the incident particle collide with a head-to-tail aggregate. The initial condition is illustrated in Fig 14(a). The incident velocity is set small as $v_{in} = 0.02 \text{ m/s}$. For two oppositely charged particles, the head-to-tail configuration appears to be less stable compared to the side-by-side configuration. Therefore, even the mild collision with $v_{in} = 0.02 \text{ m/s}$ could kick particle 1 and 2 out of the original state and initiate the restructuring (Fig 14(b)). As discussed in Section 3.2.2, particle 1 and 2 tend to stick together side-by-side to

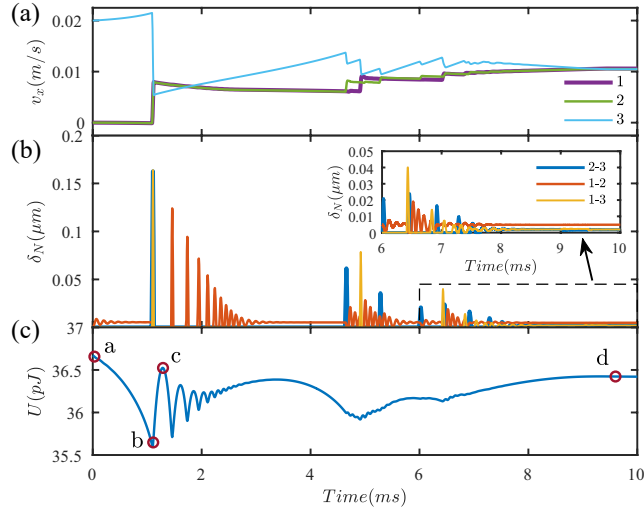


Figure 11: Temporal evolution of (a) the velocity along the x direction, (b) the inter-particle overlaps and (c) the total electrostatic energy in the collision process shown in Fig 10. The circles in (c) corresponds to different instants in Fig 10.

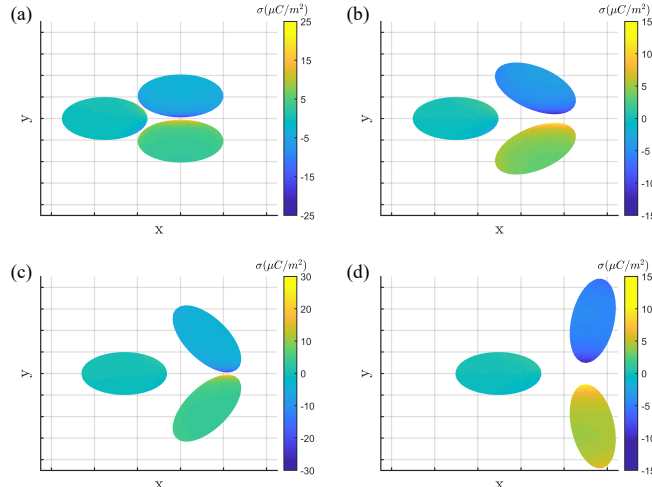


Figure 12: Snapshots of the collision process between ellipsoid 3 and the side-by-side aggregate formed by ellipsoids 1 and 2 at (a) $t = 0.15 \text{ ms}$, (b) $t = 0.72 \text{ ms}$, (c) $t = 1.2 \text{ ms}$ and (d) $t = 3 \text{ ms}$. The incident velocity of ellipsoid 3 is $v_{in} = 0.16 \text{ m/s}$ along the x direction.

reduce the electrostatic energy, so particle 3 is gradually “squeezed” out of the gap between 1 and 2. In the end, two charged particles arrange in a side-by-side configuration similar to that in Fig 10(d). The total electrostatic energy in Fig 15(c) also reduces to a lower value indicating that the present structure is more stable than the initial one.

4. Conclusion

In this study, we introduce a numerical method to perform dynamic simulations of surface-resolved dielectric particles with non-spherical shapes. The electrostatic interaction in a many-body system is calculated using the boundary element method. The GMRES-FMM coupled calculation is employed to accelerate the electrostatic calculation in each time steps. In dynamic simulations, the soft-sphere contact forces/toques are included to resolves inter-particle collisions. The reduced stiffness is applied to increase the collision time step so as to reduce the calculation cost. Besides, the double-shell model is proposed to prevent the intersection between different surface patches. To avoid introducing

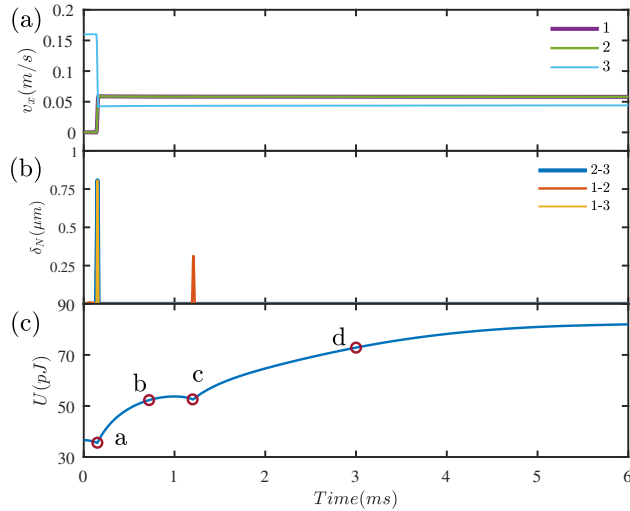


Figure 13: Temporal evolution of (a) the velocity along the x direction, (b) the inter-particle overlaps and (c) the total electrostatic energy in the collision process shown in Fig 12. The circles in (b) corresponds to different instants in Fig 12.

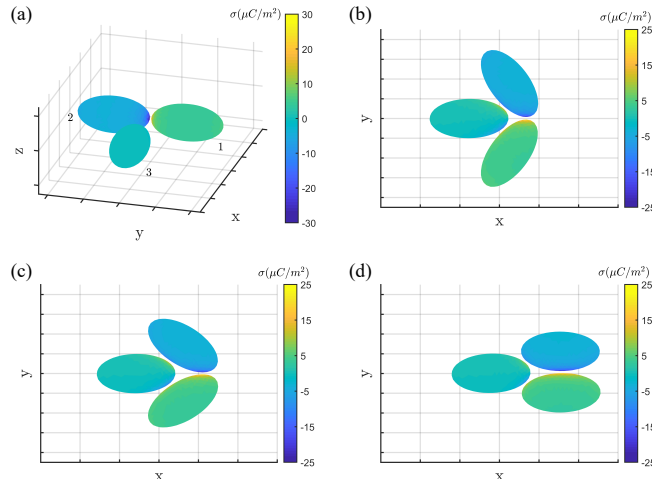


Figure 14: Snapshots of the collision process between ellipsoid 3 and the head-to-tail aggregate formed by ellipsoids 1 and 2 at (a) $t = 0.03$ ms, (b) $t = 8.10$ ms, (c) $t = 14.42$ ms and (d) $t = 23.25$ ms. The incident velocity of ellipsoid 3 is $v_{in} = 0.02$ m/s along the x direction.

extra errors in the calculation, the thickness of the buffer layer is chosen when the electrostatic energy between two close particles saturates.

By comparing the electrostatic force between two charged spheres, the effect of the induced charge is found to be significant when the surface-to-surface distance is smaller than the particle diameter. When there is particle-scale separation of the induced charge, the induced dipole could well predict the electrostatic force. However, if the induced charge is self-enhancing locally, the induced dipole model fails to capture the strong high-order multipoles. BEM is thus required for a more accurate prediction. Such phenomenon is observed between oppositely charge particles or particles carrying different amount of charge in the present study. For particles with a non-spherical shape, the induced charge may distribute non-uniformly on the particle surface. As a result, the electrostatic interactions acting on non-spherical particles become orientational. In addition, by performing dynamic simulations of particle-aggregate collisions, different collision outcomes are reproduced, including sticking, fragmentation and restructuring. The evolution of the collision process and the electrostatic interaction are also displayed to help understand the underlying

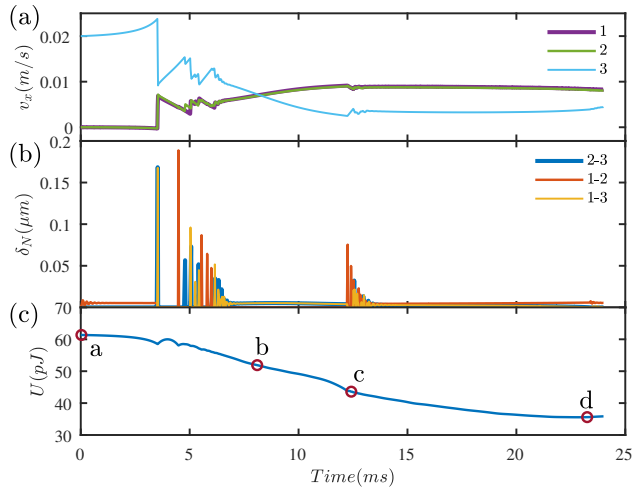


Figure 15: Temporal evolution of (a) the velocity along the x direction, (b) the inter-particle overlaps and (c) the total electrostatic energy in the collision process shown in Fig 14. The circles in (b) corresponds to different instants in Fig 14.

physics.

Based on the present study, several interesting directions may be worth pursuing. First, the present study deals with the ellipsoidal particles using the quadratic expression. By adopting other general expressions, this framework can be extended to more non-spherical shapes, e.g. arbitrary convex particles (Houlsby, 2009; Boon, Houlsby and Utili, 2013). Second, we employ the Hertz theory together with the viscoelastic dissipation force to calculate the normal contact force. For microparticles, the adhesion due to van der Waals attraction is also important for aggregation and deposition, and how the presence of the electrostatic interaction affects these processes is of interest (Li, Marshall, Liu and Yao, 2011; Jungmann, Steinpilz, Teiser and Wurm, 2018). Furthermore, the triboelectrification between dielectric particles is a long-lasting yet unsettled problem. By incorporated with certain models of charge transfer in collisions, the present framework can be applied to test different charge transfer model and help unveil the mysterious mechanism of tribocharging (McCarty and Whitesides, 2008; Lacks and Shinbrot, 2019; Kline et al., 2020).

A. Validation of the electrostatic calculation

A.1. Potential energy between a point charge and a dielectric sphere

The electrical potential energy U between a point charge q and a neutral dielectric sphere is given by Jackson (1999); Barros and Luijten (2014) as

$$U = \frac{q^2}{8\pi\epsilon_0\kappa_m R} \sum_{n=0}^{\infty} \frac{(1-\tilde{\kappa})n}{(1+\tilde{\kappa})n+1} \frac{1}{1+(d/R)^{2(n+1)}}, \quad (45)$$

where κ_m and κ_p are the dielectric constants of the medium and the sphere, $\tilde{\kappa} = \kappa_p/\kappa_m$ is their ratio. d is the distance from the point charge to the surface of the sphere, R is the sphere radius. The electrical energy U is normalized by $U_0 = q^2/\epsilon_0\kappa_m R$ and shown in Fig 16. The BEM results show good agreement with the theoretical solutions, which validates our calculation. When the point charge is close to the sphere, deviations may occur due to the limited surface patch number. Increasing the total patch number or refining the local surface patches could further improve the accuracy. Here, the total surface patch number $N_{patch} = 956$ is used to achieve high accuracy for $d/R = 0.05$.

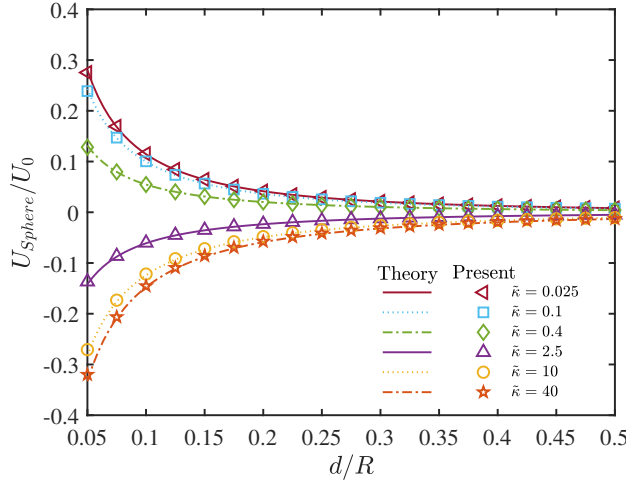


Figure 16: Normalized potential energy between a point charge and a dielectric sphere.

B. Transformation between different frames

For a point $\mathbf{x}^{(in)} = [x^{(in)}, y^{(in)}, z^{(in)}]^T$ in the inertial frame, its generalized position vector $\mathbf{X}^{(in)} = [x^{(in)}, y^{(in)}, z^{(in)}, 1]^T$ can be transformed to the co-moving frame by

$$\mathbf{X}^{(cm)} = \mathcal{T} \mathbf{X}^{(in)} \quad (46)$$

Here, the translation matrix \mathcal{T} is defined as

$$\mathcal{T} = \begin{bmatrix} 1 & 0 & 0 & -x_p^{(in)} \\ 0 & 1 & 0 & -y_p^{(in)} \\ 0 & 0 & 1 & -z_p^{(in)} \\ 0 & 0 & 0 & 1 \end{bmatrix}, \quad (47)$$

with $(x_p^{(in)}, y_p^{(in)}, z_p^{(in)})$ being the coordinates of the particle centroid in the inertial frame. The transformation between the co-moving frame and the particle frame is

$$\mathbf{X}^{(p)} = \mathcal{R} \mathbf{X}^{(cm)}. \quad (48)$$

The rotation matrix \mathcal{R} can be expressed by Euler angles (ϕ, θ, ψ) or quaternions $(\epsilon_1, \epsilon_2, \epsilon_3, \eta)$. In this study, we follow Chesnutt and Marshall (2009) and write \mathcal{R} in the form of quaternions

$$\mathcal{R} = \begin{bmatrix} 1 - 2(\epsilon_2^2 + \epsilon_3^2) & 2(\epsilon_1\epsilon_2 + \epsilon_3\eta) & 2(\epsilon_1\epsilon_3 - \epsilon_2\eta) & 0 \\ 2(\epsilon_2\epsilon_1 - \epsilon_3\eta) & 1 - 2(\epsilon_3^2 + \epsilon_1^2) & 2(\epsilon_2\epsilon_3 + \epsilon_1\eta) & 0 \\ 2(\epsilon_3\epsilon_1 + \epsilon_2\eta) & 2(\epsilon_3\epsilon_2 - \epsilon_1\eta) & 1 - 2(\epsilon_1^2 + \epsilon_2^2) & 0 \\ 0 & 0 & 0 & 1 \end{bmatrix}. \quad (49)$$

The initial values of quaternions are determined by

$$\epsilon_1 = \cos \frac{\phi - \psi}{2} \sin \frac{\theta}{2}, \quad \epsilon_2 = \sin \frac{\phi - \psi}{2} \sin \frac{\theta}{2}, \quad \epsilon_3 = \sin \frac{\phi + \psi}{2} \cos \frac{\theta}{2}, \quad \eta = \cos \frac{\phi + \psi}{2} \cos \frac{\theta}{2}. \quad (50)$$

Then quaternions are evolved by

$$\begin{bmatrix} d\epsilon_1/dt \\ d\epsilon_2/dt \\ d\epsilon_3/dt \\ d\eta/dt \end{bmatrix} = \frac{1}{2} \begin{bmatrix} \eta\Omega_x^{(p)} - \epsilon_3\Omega_y^{(p)} + \epsilon_2\Omega_z^{(p)} \\ \epsilon_3\Omega_x^{(p)} + \eta\Omega_y^{(p)} - \epsilon_1\Omega_z^{(p)} \\ -\epsilon_2\Omega_x^{(p)} + \epsilon_1\Omega_y^{(p)} + \eta\Omega_z^{(p)} \\ -\epsilon_1\Omega_x^{(p)} - \epsilon_2\Omega_y^{(p)} - \epsilon_3\Omega_z^{(p)} \end{bmatrix}. \quad (51)$$

Here $\Omega_x^{(p)}$, $\Omega_y^{(p)}$ and $\Omega_z^{(p)}$ are the components of particle's rotation rate in the particle frame.

C. Collision between ellipsoidal particles

C.1. Collision Detection

In the particle frame of the i th particle, the ellipsoid can be expressed as

$$\mathbf{X}^{(p)T} Q_i^{(p)} \mathbf{X}^{(p)} = 0. \quad (52)$$

Here $\mathbf{X}^{(p)} = [x^{(p)}, y^{(p)}, z^{(p)}, 1]^T$, the characteristic matrix of ellipsoid i is

$$Q_i^{(p)} = \begin{bmatrix} 1/a^2 & 0 & 0 & 0 \\ 0 & 1/b^2 & 0 & 0 \\ 0 & 0 & 1/c^2 & 0 \\ 0 & 0 & 0 & -1 \end{bmatrix}. \quad (53)$$

For points in the inertial frame, the coordinates can be transformed to the particle frame through $\mathbf{X}^{(p)} = \mathcal{R}\mathcal{T}\mathbf{X}^{(in)}$ (See Appendix B). Thus, in the inertial frame the ellipsoid can be written as

$$(\mathcal{R}\mathcal{T}\mathbf{X}^{(in)})^T Q_i^{(p)} (\mathcal{R}\mathcal{T}\mathbf{X}^{(in)}) = \mathbf{X}^{(in)T} \mathcal{T}^T \mathcal{R}^T Q_i^{(p)} \mathcal{R} \mathcal{T} \mathbf{X}^{(in)} = \mathbf{X}^{(in)T} Q_i^{(in)} \mathbf{X}^{(in)} = 0, \quad (54)$$

where $Q_i^{(in)} = \mathcal{T}^T \mathcal{R}^T Q_i^{(p)} \mathcal{R} \mathcal{T}$ is the 4×4 characteristic matrix of ellipsoid i in the inertial frame.

If a non-zero solution $\mathbf{X}^{(in)}$ satisfies the equation of two different ellipsoids $Q_1^{(in)}$ and $Q_2^{(in)}$, two ellipsoids intersect at $\mathbf{X}^{(in)}$. Multiplying Eq 54 of ellipsoid 1 by λ and subtracting that of ellipsoid 2 then yields

$$\mathbf{X}^{(in)T} (\lambda Q_1^{(in)} - Q_2^{(in)}) \mathbf{X}^{(in)} = 0. \quad (55)$$

Since $Q_1^{(in)}$ is invertible, $Q_1^{(in)-1} Q_2^{(in)}$ should be singular if a family of non-trivial solutions $\mathbf{X}^{(in)}$ exist. In the simulation, we check the eigen values of $Q_1^{(in)-1} Q_2^{(in)}$ for two adjacent ellipsoids. If two eigen values are complex conjugates, these two ellipsoids intersect (Alfano and Greer, 2003).

C.2. Contact Point

When two ellipsoid intersect, the contact point is identified to calculate the contact interactions. In this study, the method of level surfaces are applied for contact point identification (Ting, 1992; Džiugys and Peters, 2001; Schneider and Eberly, 2002). Eq. 54 can be expressed in the quadratic form as

$$P_i(\mathbf{x}^{(in)}) = \mathbf{x}^{(in)T} S_i^{(in)} \mathbf{x}^{(in)} + \mathbf{b}_i^{(in)T} \mathbf{x}^{(in)} + c_i^{(in)} = 0. \quad (56)$$

Here, $S_i^{(in)}$, $\mathbf{b}_i^{(in)}$ and $c_i^{(in)}$ are defined by the components of $Q_i^{(in)}$

$$S_i^{(in)} = \begin{bmatrix} q_{11}^{(in)} & q_{12}^{(in)} & q_{13}^{(in)} \\ q_{12}^{(in)} & q_{22}^{(in)} & q_{23}^{(in)} \\ q_{13}^{(in)} & q_{23}^{(in)} & q_{33}^{(in)} \end{bmatrix} \quad (57)$$

$$\mathbf{b}_i^{(in)} = 2[q_{14}^{(in)}, q_{24}^{(in)}, q_{34}^{(in)}]^T, \quad (58)$$

$$c_i^{(in)} = q_{44}^{(in)}. \quad (59)$$

The contact point on ellipsoid 1 is defined as the tangent point of ellipsoid 1 on the innermost level surface of ellipsoid 2, which is shown as $x_{C,1}$ in Fig 5. The level surfaces of ellipsoid 2 is given by

$$P_2(\mathbf{x}^{(in)}) = \alpha, \quad (60)$$

where $\alpha < 0$ and $\alpha > 0$ corresponds to the interior and exterior of ellipsoid 2. Then finding the contact point is equivalent to finding the minimum value of α in Eq 60 under the constraint of $P_1(\mathbf{x}^{(in)}) = 0$. By defining the Lagrangian function

$$\mathcal{L}(\mathbf{x}^{(in)}) = P_2(\mathbf{x}^{(in)}) + \tau P_1(\mathbf{x}^{(in)}) \quad (61)$$

for optimization, the contact point $\mathbf{x}_{C,1}^{(in)}$ is given by

$$\mathbf{x}_{C,1}^{(in)} = -\frac{1}{2}(S_2^{(in)} + \tau S_1^{(in)})^{-1}(\mathbf{b}_2^{(in)} + \tau \mathbf{b}_1^{(in)}) = \frac{1}{\Phi(\tau)}\mathbf{y}(\tau), \quad (62)$$

where $\Phi(\tau) = \det(S_2^{(in)} + \tau S_1^{(in)})$ is the determinant of $(S_2^{(in)} + \tau S_1^{(in)})$. τ is the Lagrangian multiplier that can be obtained from the following six-order polynomial

$$\mathbf{y}(\tau)^T S_1^{(in)} \mathbf{y}(\tau) + \Phi(\tau) \mathbf{b}_1^{(in)T} \mathbf{y}(\tau)^T + \Phi^2(\tau) c_1 = 0. \quad (63)$$

The above process can be repeated to identify the contact point $x_{C,2}$ of ellipsoid 2 on the level surfaces of ellipsoid 1 (for details, see Chesnutt and Marshall (2009)).

D. Simulation acceleration using the reduced particle stiffness

In dynamic simulations of soft spheres, the smallest time scale is the collision time scale, which scales as $\tau_C \sim [m^2/(E^2 R v_0)]^{1/5}$. In order to accurately resolve the collision process, the fine collision time step $\Delta t_C = f_C \tau_C$ is required where f_C is much smaller than unity (Marshall, 2009; Li et al., 2011). For micron solid particles, if the real value of the elastic modulus E is used, the calculation will become extremely expensive due to the ultra-small collision time scale. Therefore, the elastic modulus is often reduced from its original value, so that a larger time step Δt_C can be used to resolve a certain process (Behjani, Rahamanian, Fardina bt Abdul Ghani and Hassanpour, 2017; Chen, Liu and Li, 2019; Ruan, Chen and Li, 2020). To avoid any unphysical effects of the reduced stiffness, other forces acting on the particles should also be modified (Hærvig, Kleinhans, Wieland, Spliethoff, Jensen, Sørensen and Condra, 2017; Washino, Chan and Tanaka, 2018).

In this appendix, the linear momentum equation is nondimensionalized in presence of the electrostatic force. The guideline of adjusting the electrostatic force is then given when a reduced elastic modulus is used. When a charged particle encounters a head-on collision, the linear momentum equation (Eq 20) is

$$m \frac{d\mathbf{v}}{dt} = -(k_N \delta_N + \eta_N v_{rel,n}) \mathbf{n} + \mathbf{F}_E. \quad (64)$$

We introduce the dimensionless velocity $\hat{\mathbf{v}}$ and the dimensionless overlap $\hat{\delta}_N$ as

$$\hat{\mathbf{v}} = \mathbf{v}/v_0, \quad (65a)$$

Parameters	Values	Units
Radius, R	100	μm
Buffer layer thickness, δ_{bl}	5	μm
Particle density, ρ_p	2500	kg/m^3
Free charge density, σ_f	± 6.4	$\mu C/m^2$
Original elastic modulus, E_0	1×10^9	Pa
Reduced ratio, χ	$1, 1.76 \times 10^{-1}, 3.13 \times 10^{-2}, 5.52 \times 10^{-3}$	—
Dielectric constant of particle, κ_p	10	—
Dielectric constant of medium, κ_m	1	—
Restitution coefficient, e	0.7	—

Table 3

Simulation parameters for reduced stiffness tests.

$$\hat{\delta}_N = \delta_N / \delta_0. \quad (65b)$$

Here, the approaching velocity between two colliding particles is chosen as the characteristic velocity v_0 , while the characteristic overlap is given by

$$\delta_0 = \left(\frac{mv_0^2}{ER^{1/2}} \right)^{2/5}. \quad (66)$$

Then Eq 64 becomes

$$\frac{d\hat{\mathbf{v}}}{dt} + \frac{4}{3}\hat{\delta}_N^{3/2}\mathbf{n} + \frac{2}{\sqrt{3}}\alpha_N\hat{\delta}_N^{1/4}\hat{v}_{rel,n}\mathbf{n} = \left(\frac{1}{m^3 v_0^6 E^2 R} \right)^{1/5} \mathbf{F}_E. \quad (67)$$

After choosing a reduced elastic modulus E_R , the dimensionless electrostatic force

$$\hat{\mathbf{F}}_E = \left(\frac{1}{m^3 v_0^6 E^2 R} \right)^{1/5} \mathbf{F}_E \quad (68)$$

should remain unchanged, so that Eq 67 gives the correct results. Thus, the dimensional electrostatic force should be modified as

$$\mathbf{F}_{E,R} = \left(\frac{E_R}{E_O} \right)^{2/5} \mathbf{F}_{E,O} = \chi^{2/5} \mathbf{F}_{E,O}. \quad (69)$$

Here, the subscripts O and R denote variables in a case with the original stiffness and that in a reduced case, respectively. $\chi = E_R/E_O$ is the reduced ratio. The electrostatic torque is also adjusted in a similar way. It is worthy to note that, the electrostatic force and torque are *only* modified in a collision process. When particles do not contact, particle movements are evolved using the original values of F_E and M_E .

The test cases of a binary collision are given here. Two spheres carrying opposite charge are released at $(0, 0, 0)$ and $(2.5R, 0, 0)$. Simulation parameters are listed in Table 3. Due to the electrostatic attraction, two spheres start to approach each other and collide. Fig 17 displays the temporal evolution of the normal overlap and the normal relative velocity. Both the collision duration and the maximum overlap increase with a smaller reduced ratio χ . As shown in the insets, when normalized by δ_0 (or v_0) and $T_C = \delta_0/v_0$, the dimensionless curves coincide, which indicates that Eq 67 gives the same results for different χ . Therefore, reducing the stiffness does not alter the collision outcomes.

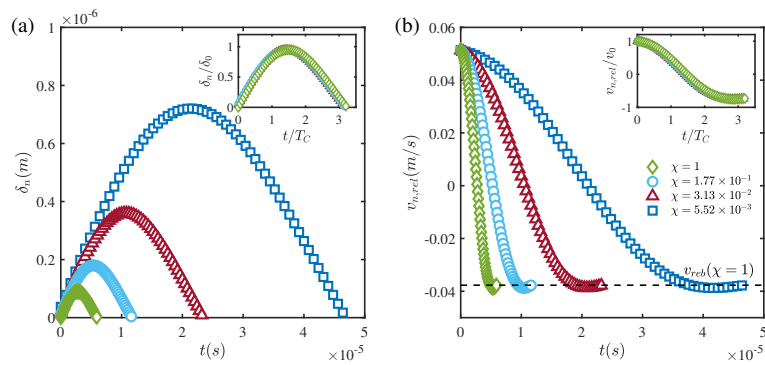


Figure 17: (a) Normal overlap and (b) normal relative velocity between two oppositely charged particles in a head-on collision with modified electrostatic force.

References

- Alfano, S., Greer, M.L., 2003. Determining if two solid ellipsoids intersect. *Journal of Guidance, Control, and Dynamics* 26, 106–110. doi:10.2514/2.5020.
- Allahyarov, E., Zaccarelli, E., Sciortino, F., Tartaglia, P., Löwen, H., 2007. Interaction between charged colloids in a low dielectric constant solvent. *EPL (Europhysics Letters)* 78, 38002.
- Barros, K., Luijten, E., 2014. Dielectric effects in the self-assembly of binary colloidal aggregates. *Phys. Rev. Lett.* 113, 017801. URL: <https://link.aps.org/doi/10.1103/PhysRevLett.113.017801>, doi:10.1103/PhysRevLett.113.017801.
- Barros, K., Sinkovits, D., Luijten, E., 2014. Efficient and accurate simulation of dynamic dielectric objects. *The Journal of Chemical Physics* 140, 064903. doi:10.1063/1.4863451.
- Behjani, M.A., Rahamanian, N., Fardina bt Abdul Ghani, N., Hass nanopour, A., 2017. An investigation on process of seeded granulation in a continuous drum granulator using dem. *Advanced Powder Technology* 28, 2456–2464. doi:<https://doi.org/10.1016/j.apt.2017.02.011>.
- Bichoutskaia, E., Boatwright, A.L., Khachatourian, A., Stace, A.J., 2010. Electrostatic analysis of the interactions between charged particles of dielectric materials. *The Journal of chemical physics* 133, 024105.
- Boon, C., Houslsby, G., Utili, S., 2013. A new contact detection algorithm for three-dimensional non-spherical particles. *Powder technology* 248, 94–102.
- Chen, S., Liu, W., Li, S., 2019. A fast adhesive discrete element method for random packings of fine particles. *Chemical Engineering Science* 193, 336–345. URL: <https://www.sciencedirect.com/science/article/pii/S0009250918306754>, doi:<https://doi.org/10.1016/j.ces.2018.09.026>.
- Chesnutt, J., Marshall, J., 2009. Blood cell transport and aggregation using discrete ellipsoidal particles. *Computers and Fluids* 38, 1782–1794.
- Di Renzo, M., Urzay, J., 2018. Aerodynamic generation of electric fields in turbulence laden with charged inertial particles. *Nature communications* 9, 1–11.
- Džiugys, A., Peters, B., 2001. An approach to simulate the motion of spherical and non-spherical fuel particles in combustion chambers. *Granular matter* 3, 231–266.
- Feng, J.Q., 2000. Electrostatic interaction between two charged dielectric spheres in contact. *Physical Review E* 62, 2891.
- Greengard, L., Rokhlin, V., 1987. A fast algorithm for particle simulations. *Journal of computational physics* 73, 325–348.
- Güttler, C., Blum, J., Zsom, A., Ormel, C.W., Dullemond, C.P., 2010. The outcome of protoplanetary dust growth: pebbles, boulders, or planetesimals? i. mapping the zoo of laboratory collision experiments. *Astronomy & Astrophysics* 513, A56.
- Haervig, J., Kleinhans, U., Wieland, C., Spliethoff, H., Jensen, A.L., Sørensen, K., Condra, T.J., 2017. On the adhesive jkr contact and rolling models for reduced particle stiffness discrete element simulations. *Powder Technology* 319, 472–482.
- Harper, J.M., McDonald, G., Dufek, J., Malaska, M., Burr, D., Hayes, A., McAdams, J., Wray, J., 2017. Electrification of sand on titan and its influence on sediment transport. *Nature Geoscience* 10, 260–265.
- Houslsby, G., 2009. Potential particles: a method for modelling non-circular particles in dem. *Computers and Geotechnics* 36, 953–959.
- Jackson, J., 1999. Classical Electrodynamics. Wiley.
- Jaworek, A., Marchewicz, A., Sobczyk, A., Krupa, A., Czech, T., 2018. Two-stage electrostatic precipitators for the reduction of pm2.5 particle emission. *Progress in Energy and Combustion Science* 67, 206–233.
- Jones, J., 1995. Electromechanics of Particles. Cambridge University Press.
- Jungmann, F., Steinpilz, T., Teiser, J., Wurm, G., 2018. Sticking and restitution in collisions of charged sub-mm dielectric grains. *Journal of Physics Communications* 2, 095009.
- Kline, A.G., Lim, M.X., Jaeger, H.M., 2020. Precision measurement of tribocharging in acoustically levitated sub-millimeter grains. *Review of Scientific Instruments* 91, 023908.
- Kolehmainen, J., Ozel, A., Gu, Y., Shinbrot, T., Sundaresan, S., 2018. Effects of polarization on particle-laden flows. *Physical review letters* 121, 124503.
- Lacks, D.J., Shinbrot, T., 2019. Long-standing and unresolved issues in triboelectric charging. *Nature Reviews Chemistry* 3, 465–476.
- Lee, V., Waitukaitis, S.R., Miskin, M.Z., Jaeger, H.M., 2015. Direct observation of particle interactions and clustering in charged granular streams.

- Nature Physics 11, 733–737.
- Li, S., Marshall, J.S., Liu, G., Yao, Q., 2011. Adhesive particulate flow: The discrete-element method and its application in energy and environmental engineering. *Progress in Energy and Combustion Science* 37, 633–668.
- Lindell, I.V., Sten, J.C.E., Nikoskinen, K.I., 1993. Electrostatic image method for the interaction of two dielectric spheres. *Radio science* 28, 319–329.
- Lindgren, E.B., Stace, A.J., Polack, E., Maday, Y., Stamm, B., Besley, E., 2018a. An integral equation approach to calculate electrostatic interactions in many-body dielectric systems. *Journal of Computational Physics* 371, 712–731. doi:<https://doi.org/10.1016/j.jcp.2018.06.015>.
- Lindgren, E.B., Stamm, B., Maday, Y., Besley, E., Stace, A.J., 2018b. Dynamic simulations of many-body electrostatic self-assembly. *Philosophical Transactions of the Royal Society A: Mathematical, Physical and Engineering Sciences* 376, 20170143.
- Liu, G., Marshall, J., Li, S., Yao, Q., 2010. Discrete-element method for particle capture by a body in an electrostatic field. *International Journal for Numerical Methods in Engineering* 84, 1589–1612.
- Lu, J., Shaw, R.A., 2015. Charged particle dynamics in turbulence: Theory and direct numerical simulations. *Physics of Fluids* 27, 065111.
- Marshall, J., 2009. Discrete-element modeling of particulate aerosol flows. *Journal of Computational Physics* 228, 1541–1561. doi:<https://doi.org/10.1016/j.jcp.2008.10.035>.
- Matias, A., Shinbrot, T., Araújo, N., 2018. Mechanical equilibrium of aggregates of dielectric spheres. *Physical Review E* 98, 062903.
- McCarty, L.S., Whitesides, G.M., 2008. Electrostatic charging due to separation of ions at interfaces: contact electrification of ionic electrets. *Angewandte Chemie International Edition* 47, 2188–2207.
- Nakajima, Y., Sato, T., 1999. Calculation of electrostatic force between two charged dielectric spheres by the re-expansion method. *Journal of Electrostatics* 45, 213–226. doi:[https://doi.org/10.1016/S0304-3886\(98\)00051-5](https://doi.org/10.1016/S0304-3886(98)00051-5).
- Ohshima, H., 1995. Electrostatic interaction between two dissimilar spheres with constant surface charge density. *Journal of colloid and interface science* 170, 432–439.
- Ohshima, H., Mishonova, E., Alexov, E., 1996. Electrostatic interaction between two charged spherical molecules. *Biophysical chemistry* 57, 189–203.
- Persson, P.O., Strang, G., 2004. A simple mesh generator in matlab. *SIAM Review* 46, 329–345.
- Qin, J., de Pablo, J.J., Freed, K.F., 2016. Image method for induced surface charge from many-body system of dielectric spheres. *The Journal of chemical physics* 145, 124903.
- Ruan, X., Chen, S., Li, S., 2020. Structural evolution and breakage of dense agglomerates in shear flow and taylor-green vortex. *Chemical Engineering Science* 211, 115261. doi:<https://doi.org/10.1016/j.ces.2019.115261>.
- Ruan, X., Chen, S., Li, S., 2021. Effect of long-range coulomb repulsion on adhesive particle agglomeration in homogeneous isotropic turbulence. *Journal of Fluid Mechanics* 915.
- Schneider, P., Eberly, D.H., 2002. Geometric tools for computer graphics. Elsevier.
- Song, D., Mehrani, P., 2017. Mechanism of particle build-up on gas-solid fluidization column wall due to electrostatic charge generation. *Powder technology* 316, 166–170.
- Steinpilz, T., Joeris, K., Jungmann, F., Wolf, D., Brendel, L., Teiser, J., Shinbrot, T., Wurm, G., 2020. Electrical charging overcomes the bouncing barrier in planet formation. *Nature Physics* 16, 225–229.
- Telling, J., Dufek, J., Shaikh, A., 2013. Ash aggregation in explosive volcanic eruptions. *Geophysical Research Letters* 40, 2355–2360.
- Ting, J.M., 1992. A robust algorithm for ellipse-based discrete element modelling of granular materials. *Computers and Geotechnics* 13, 175–186.
- Washino, K., Chan, E.L., Tanaka, T., 2018. Dem with attraction forces using reduced particle stiffness. *Powder Technology* 325, 202–208.
- Washizu, M., 1993. Precise calculation of dielectrophoretic force in arbitrary field. *Journal of electrostatics* 29, 177–188.